Acoustically induced current in graphene by aluminum nitride transducers

Yan Chen,[a)] Hongxiang Zhang,[a)] Hao Zhang, Zhihong Feng, Hongyuan Zhao,
Chongling Sun, Shijun Zheng, Wei Pang,[b)] and Daihua Zhang[c)]
State Key Laboratory of Precision Measuring Technology and Instruments, Tianjin University, Tianjin 300072, China

We report on the excitation of acousto-eletric (AE) charge transport in monolayer graphene by acoustic transducers based on aluminum nitride thin films. The acoustic waves induced macroscopic current flow that linearly scaled with input power. The AE current exhibited unique frequency dependence due to special configuration and piezoelectric properties of the transducer, which led to transitions between traveling and standing acoustic waves across a characteristic frequency. A Finite Element model was built to investigate and understand the phenomena and the underlying mechanisms. © 2016 AIP Publishing LLC. [http://dx.doi.org/10.1063/1.4940400]

AE effect originates from interactions of charge carriers and acoustic waves propagating in low-dimensional systems. It provides an effective tool to investigate the electronic and phononic behaviors of low-dimensional materials and structures,[1] and enables a variety of potential applications ranging from single electron manipulation,[2] surface defects detection, tunable surface acoustic wave (SAW) device,[3] to chemical[4] and opto-electrical sensors.[5] Studies in the past decades have primarily focused on two different device platforms. The first one leverages two-dimensional electron gases (2DEGs) formed at the interfaces of semiconductor heterostructures. The configuration has enabled numerous breakthroughs, including the realisation of controlled single electron tunnelling between well-separated quantum dots. However, since the semiconducting materials that can be used in such systems are weakly piezoelectric, the resultant AE effects were generally very weak, often requiring ultralow temperature to be detected. The second platform involves one-dimensional (1D)[6] or two-dimensional (2D)[2] nanomaterials intimately attached to a piezoelectric substrate, which couples acoustic waves into the semiconducting or semi-metallic nanostructures. Single-crystal lithium niobate ($LiNbO_3$) has been the most favourite substrate used in this case, and a wide variety of nanomaterials, including carbon nanotubes,[7] GaN[8] and GaAs nanowires,[9] graphene[1,2,4] and few-layered MoS_2,[10] have been systematically investigated. Due to large piezoelectric coefficient of $LiNbO_3$ and high carrier mobilities of the nanomaterials, this platform creates well observable AE effects at room temperature, and has become increasingly prevalent ever since the emergence of 1D and 2D nanomaterials.

In spite of the strong piezoelectricity of $LiNbO_3$, the material imposes a number of limitations at the same time. First of all, the working frequency of typical $LiNbO_3$ transducers ranges from 30 to 400 MHz. They can hardly operate at gigahertz frequency or above due to intrinsic limitations of the material and micro-fabrication processes. This has largely hindered the exploration and development of AE devices in

high frequency regeme. Second, the fabrication of $LiNbO_3$ devices is not compatible with that of integrated circuits (IC), making it impossible to integrate peripheral and other functional devices on the same chip. Furthermore, unlike thin-film piezoelectric devices built on silicon wafers, the $LiNbO_3$ substrate does not support vertical integration for added functionality and device density. Its anisotropic properties along different in-plane directions add another layer of complexity and limitation to device design and fabrication.

In this study, we demonstrated a unique device structure by incorporating monolayer graphene film with an AlN-based acoustic transducer. The device exhibited macroscopic AE current at room temperature with typical current density of $11\,nA/\mu m$ at an input power of $10\,dBm$. The current varied with both the frequency and amplitude of the acoustic waves. Contrary to typical $LiNbO_3$ based devices, the AE current reached minimum at resonance due to the formation of standing waves. A Finite-Element model was constructed to systematically explain the generation and propogation of the acoustic waves responsible for the observed AE effect. The piezoelectric AlN thin film serves as a good alternative to $LiNbO_3$ and opens up more possibilities for the studies and applications of this area.

Figure 1(a) shows the schematic of the AE device, which consists of an AlN solidly mounted resonator (SMR) and a monolayer graphene sheet attached to the surface. Fabrication of the SMR started from the underlying Bragg reflector, formed by 3 pairs of alternating AlN/SiO_2 layers deposited successively by physical and chemical vapor depositions. Thicknesses of the layers were 1200/700, 1000/1300, and 1000/650 nm from bottom to top. The Bragg reflector minimizes energy dissipation to Si substrate, having the acoustic waves retained within the upper section of the device. The bottom electrode (BE), the top electrodes (TIE and TOE), and the piezoeletric layer sandwiched in between are responsible for the excitation of acoustic waves. Thickness and material of the layers determine key parameters of the SMR, including its impedance, resonant frequencies, and effective coupling coefficient. The specific BE/piezo/TIE stack was configured to be 600 nm Molybdenum/1000 nm AlN/300 nm Au in our case. The bottom and top electrodes

a)Y. Chen and H. Zhang contributed equally to this work.
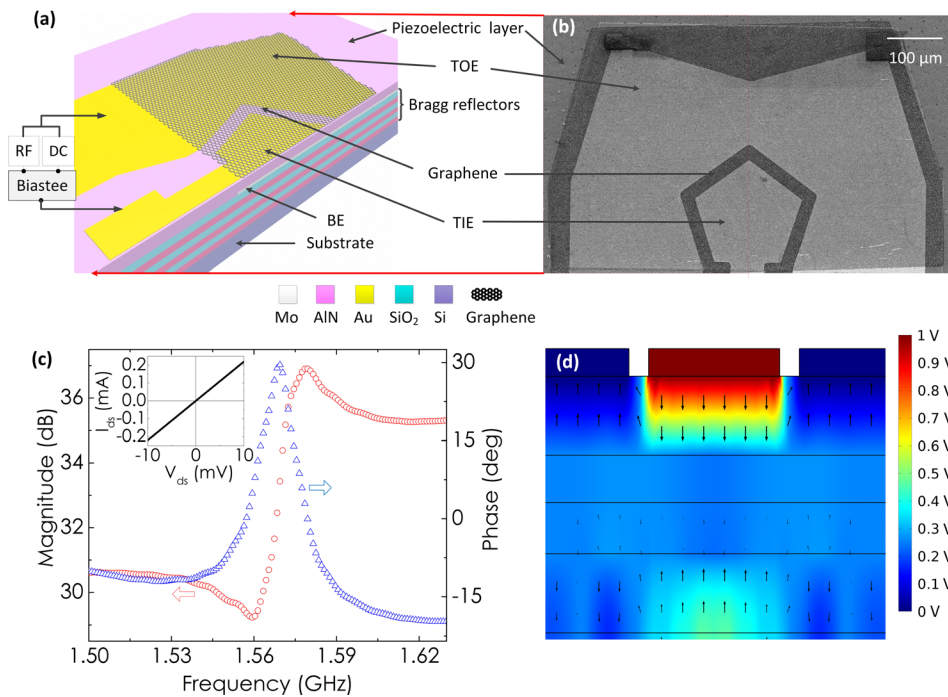b)E-mail: weipang@tju.edu.cn
c)E-mail: dhzhang@tju.edu.cn

FIG. 1. (a) Cross-sectional schematic of the graphene/AlN hybrid device. In a typical measurement, the RF and DC source meters were connected to the two Au electrodes (labeled as TIE and TOE) through a Bias-Tee. (b) Top view SEM image showing the contour of the entire device. (c) Magnitude (red) and phase (blue) of impedance over frequency. The series and parallel resonance occurred at 1.56 and 1.58 GHz, respectively. Inset: DC current vs. voltage between TIE and TOE. (d) Finite Element simulation showing the electric potential (color plot) and field (arrows) distribution within different layers.

were patterned using dry etching and liftoff processes, respectively. Deposition of the piezoelectric layer was under strict process control with well-optimized parameters, which resulted in homogeneous and uniform c-axis AlN film with good crystallinity and excellent piezoelectric properties. A sharp peak was present in the X-ray diffraction spectrum at (002) with a Full-Width-at-Half-Maximum (FWHM) of 1.5°.[11] The strong piezoelectricity of the film has enabled the demonstration of a series of high-performance Bulk Acoustic Wave (BAW) and Contour Mode Resonators (CMRs) in our previous studies.[11,12]

A monolayer graphene film was then transferred onto the substrate after completion of the SMR. Details of the transfer process and parameter settings can be found elsewhere.[13] The well-engineered techniques ensured strong and wrinkle-free adhesion of the graphene film to the substrate through Van der Waals interactions with the substrate. The graphene was then trimmed using oxygen plasma to within the active area of the SMR to avoid undesired coupling with neighboring devices. E-beam lithography was used for patterning to minimize process-induced surface contaminations that were commonly observed in photolithography.[14] The scanning electron microscopy (SEM) image in Fig. 1(b) shows clear countours of the graphene film and the top electrodes. The bottom electrode was buried under the AlN layer and is therefore unseen from this image.

For electrical characterizations, the SMR/graphene hybrid device was mounted onto an evaluation board with the TIE and TOE connected to the center pin and outer shell of a co-axial small-A-type (SMA) connector. The board was then connected to a Bias-Tee to decouple radio frequency (RF) and direct-current (DC) signals from each other.[15] This allowed us to probe the two devices connected in parallel— the SMR and the graphene film independently and simultaneously. In the last step, the RF and DC outputs from the Bias-Tee were hooked up to a network analyzer (Agilent E5071B) and a DC source meter (Agilent B1500),

respectively. Figure 1(c) and the inset summarize the characterization results of both devices. The red and blue curves plot the magnitude and phase of the SMR impedance with varying frequency from 1.50 to 1.63 GHz. The hybrid device behaved essentially the same as a bare SMR in RF characteristics. The valley and peak of the impedance magnitude at 1.56 and 1.58 GHz correspond to the series and parallel resonance of the thickness extension (TE) mode. It is interesting to note that even the RF bias was applied across two laterally placed electrodes; the electric field was essentially in the vertical direction due to the equipotential surface on the floating BE, as illustrated in the simulation result in Fig. 1(d). The DC characteristic of the device was primarily dominated by the graphene film, a p-type semiconducting channel bridging the two top electrodes. The linear current vs. voltage (I-V) curve in Fig. 1(c) inset indicates formation of metallic contacts at the graphene/metal interface.

In the following paragraph we focus on the AE characteristics of the hybrid device, that is, the DC current as a function of varying frequency and input power. The experimental data are shown in Fig. 2(a). A DC bias of +5 mV was applied between the TIE and TOE, which induced a background DC current of ~114.5 μA throughout all the measurements. Each individual curve was taken at different RF powers of −10, 0, 5, 8, and 10 dBm, respectively. At −10 dBm, the input power was insufficient to produce any detectable AE current; therefore, the signal was contributed solely from the background DC current in this case, and remained constant across the frequency range (orange curve). As the input power increased, two features started to emerge. First, the current level rose monotonically due to the onset of AE effect. Figure 2(b) plots the current with varying RF power at three different frequencies. At each frequency, the current scaled linearly with the input power. The linear relationship is highly consistent with previous observations in LiNbO$_3$ devices[1,5] and considered to be a signature feature of AE current. Second, in the measurement shown in
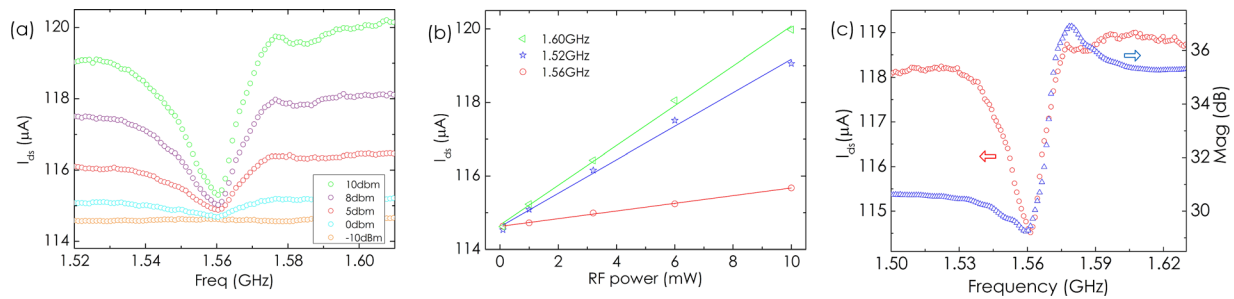
FIG. 2. (a) DC current between TIE and TOE as a function of driving frequency. The curves were taken at different input powers from −10 to 10 dBm. (b) DC current vs. input power at different frequencies. (c) DC current (red) and impedance (blue) of the hybrid device were simultaneously recorded during a frequency scan from 1.50 to 1.63 GHz, showing that the AE current reached minimum at the series resonance of the acoustic transducer.

Fig. 2(a), the DC current dropped collectively at 1.56 GHz regardless of the input power. The frequency corresponds to the series resonance of the SMR as illustrated in Fig. 2(c). This unique feature results from the specific piezoelectric properties of our device and has never been observed in previous studies. Finite element simulations found a traveling acoustic wave between the two electrodes that had minimum energy flux at the series resonance frequency (f_s) of the SMR. This is most probably the root cause of the unexpected current drop at f_s. Detailed analysis will be elaborated in a later paragraph.

Figure 3 presents more experimental results to better understand our observations. In the first test shown in Fig. 3(a), we repeated the current vs. frequency (I-f) measurement with different DC biases applied to the device at 5, 0, and −5 mV, respectively. The frequency response of all three measurements is essentially the same except for a constant offset induced by the DC bias. The results indicate that the AE current was sufficiently large and highly robust even in the presense of a counter flow of electrically induced current. The test also ruled out the possiblity of piezo-resistive effect, as the direction and magnitude of the change in current remained the same regardless of the polarity of the DC bias. Figure 3(b) describes the idea of another experiment, in which the two RF terminals were swapped with each other between two consecutive I-f measurements. The two configurations resulted in very similar curves (Fig. 3(c)), indicating that the direction and frequency response of the current were independent of the RF terminal arrangement. This is an important verification particularly to our setup, where the SMR

and the graphene film shared the same electrodes. One needs to take extreme caution in experimental design and data analysis to avoid possible artifacts induced by crosstalks between the RF and DC signals. The result shown in Fig. 3(c) proves that the observed DC current was indeed an outcome of the AE interactions between the SMR and the graphene film, rather than interference from internal or external electronics.

AE currents in graphene and other 2D nanomaterials have been observed and discussed in a number of literatures.[1,4,5,16] A widely accepted model attributed the acoustically induced charge transport to periodic modulation of electronic energy bands in the atomically-thin film by longitudinal strain waves. A steady travelling wave is required in this case to carry the charge carriers inside the semiconducting channel from one end to the other. However, it is an open question whether and how a traveling wave can arise and propagate on the surface of our SMR device, which is generally designed for the resonance of standing acoustic waves in TE mode. We therefore built a finite element model to examine the surface longitudinal waves on the SMR, particularly in the region between the two top electrodes. To further simplify the discussion, we focused solely on the strain waves along the 1D segment normal to the edge of the electrodes (defined as x direction, positive when pointing from inside to outside), as highlighted in Fig. 4(a).

Figures 4(b) and 4(c) plot the longitudinal displacement (x-component) of the waves at different positions along the line. The data were taken at four different phases within one period, at $\pi/4$, $2\pi/4$, $3\pi/4$, and π, respectively. Figure 4(b) is
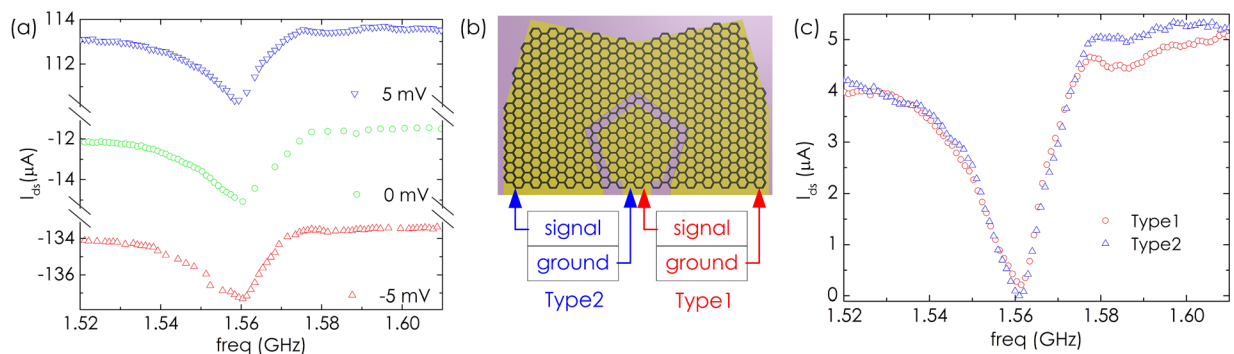

FIG. 3. (a) Frequency dependence of the AE current (positive direction is defined as a flow from the inner to the outer Au electrode) recorded at different DC biases between the two electrodes. (b) Schematic of two different test configurations. In Type 1, the inner and outer electrodes were connected to the signal and ground terminals of the network analyzer, respectively, while Type 2 swapped the two terminals. (c) The DC current of the two configurations were essentially the same in both direction and magnitude.
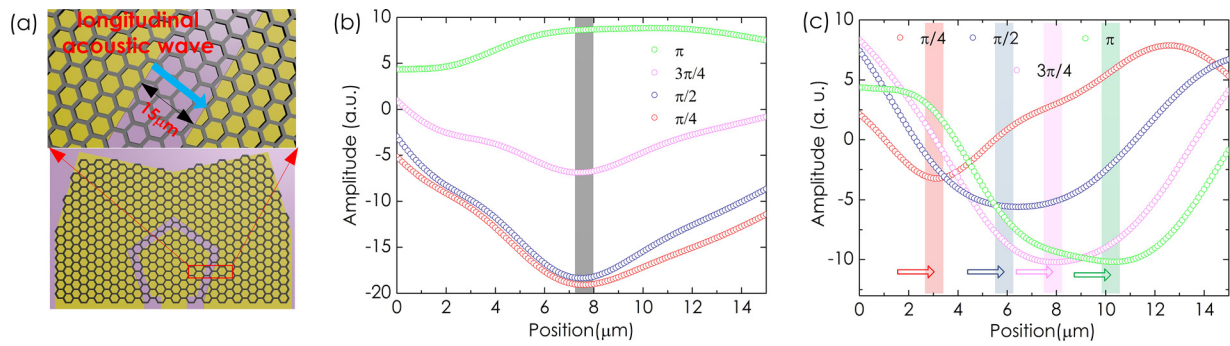
FIG. 4. Finite Element simulation results. The model investigated the strain waves propagating between the inner and outer electrodes within the 15 μm-wide gap highlighted in (a). (b) Strain wave profiles taken at different phases varying from π/4 to π with π/4 interval. At 1.56 GHz, the four wave antinodes occurred at the same location, approximately 7.5 μm from the edge of the inner electrode. (c) Wave profiles at 1.50 GHz. The antinode migrated from left to right over time, indicating a travelling wave.

the result at f_s and Fig. 4(c) for typical off-resonance situations. Comparison between the two figures reveals an interesting and important difference. At f_s, the antinodes of different phases keep at approximately the same position, as how a standing acoustic wave would behave, while at frequencies other than f_s, the antinode continuously shifts towards +x direction, indicating the onset of a traveling wave. The simulation results perfectly explain the unique frequency dependence in Fig. 2(a), where the AE current reached minimum at f_s when the traveling wave on the SMR transitioned fully or partially to a standing wave. According to our simulation, the direction of the traveling wave is always pointing from the inner to the outer electrode regardless of frequency. This is well consistent with the direction of the measured DC current that was conducted by holes in p-type doped graphene films. It is also worth mentioning that both the standing and the traveling waves are essentially composite waves consisted of multiple harmonic components with different wavelengths. The amplitude of the wave is therefore not a constant along the x axis.

According to the simulation results, the longitudinal component of the traveling waves along the SMR surface behaves essentially the same as typical SAWs in LiNbO₃. We can therefore borrow the equations of SAW devices[5] to take a semi-quantitative analysis for the AE current observed in our setup. At frequencies sufficiently apart from f_s (e.g., <1.54 or >1.58 GHz), the AE current scales linearly with frequency and the carrier mobility of graphene, and can be written in the following form:

$$I = \mu P_l f \frac{k_{eff}^2 \pi}{\nu^2}\left[\frac{\sigma_g/\sigma_{AlN}}{1+\left(\sigma_g/\sigma_{AlN}\right)^2}\right], \quad (1)$$

where, μ is the hole mobility in monolayer graphene, estimated to be 200–1000 cm²/(Vs) for typical chemical vapor deposition grown samples,[17] f is the frequency and set to be 1.50 GHz in the following approximation, P_l was defined as the power of SAW in Ref. 5, which corresponds to the power of the traveling longitudinal waves in our case. As the traveling waves contribute to a significant portion of the power loss in the SMR, we can use $P_l = P/Q_{SMR}$, with P being the total input power and Q_{SMR} the quality factor of the SMR to approximate the power carried by the traveling waves. At $P = 10$ dBm and $Q_{SMR} = 60$, $P_l = 0.17$ mW. k_{eff}^2 is the

effective piezoelectric coupling coefficient of the SMR, approximately 3% according to our previous characterizations,[18] ν is the speed of acoustic wave and approximately 4000 m/s, and $\sigma_g \approx 9 \times 10^{-6}$ S and $\sigma_{AlN} = 4 \times 10^{-7}$ S are the characteristic conductivities of graphene and AlN, respectively. Plugging the numbers into Eq. (1) results in an AE current of 1.3–6.5 μA, in the same order with our experimental result of ∼4 μA at 10 mW input power. We have proved both experimentally and theoretically that the AlN SMR is able to produce comparable level of AE current as that of LiNbO₃ devices. In fact, since their working frequency is significantly higher than typical SAWs, the AlN SMRs are expected to deliver even higher performance in power efficiency and frequency bandwidth after more careful and systematic engineering.

In summary, we demonstrated use of AlN-based SMR to produce macroscopic AE current in monolayer graphene film. We observed very unique frequency dependence of the AE current, and developed a Finite Element model to understand the physical behaviors and underlying mechanisms. This is the first demonstration of AlN based AE device with IC-compatible fabrication processes. Our work proposed a unique material set and device configuration, which would open up more opportunities for the studies and applications of AE effects and devices.

[1]V. Miseikis, J. E. Cunningham, K. Saeed, R. O'Rorke, and A. G. Davies, Appl. Phys. Lett. **100**(13), 133105 (2012).
[2]R. P. McNeil, M. Kataoka, C. J. Ford, C. H. Barnes, D. Anderson, G. A. Jones, I. Farrer, and D. A. Ritchie, Nature **477**(7365), 439 (2011).
[3]R. Li, P. I. Reyes, S. Ragavendiran, H. Shen, and Y. Lu, Appl. Phys. Lett. **107**(7), 073504 (2015).
[4]Z. Insepov, E. Emelin, O. Kononenko, D. V. Roshchupkin, K. B. Tnyshtykbayev, and K. A. Baigarin, Appl. Phys. Lett. **106**(2), 023505 (2015).
[5]T. Poole, L. Bandhu, and G. R. Nash, Appl. Phys. Lett. **106**(13), 133107 (2015).
[6]Y. C. Chen, X. Y. Ding, S. C. S. Lin, S. K. Yang, P. H. Huang, N. Nama, Y. H. Zhao, A. A. Nawaz, F. Guo, W. Wang, Y. Y. Gu, T. E. Mallouk, and T. J. Huang, ACS Nano **7**(4), 3306 (2013).
[7]J. Ebbecke, C. J. Strobl, and A. Wixforth, Phys. Rev. B **70**, 233401 (2004).

[8]J. Ebbecke, S. Maisch, A. Wixforth, R. Calarco, R. Meijers, M. Marso, and H. Luth, Nanotechnology **19**(27), 275708 (2008).

[9]J. B. Kinzel, D. Rudolph, M. Bichler, G. Abstreiter, J. J. Finley, G. Koblmuller, A. Wixforth, and H. J. Krenner, Nano Lett. **11**(4), 1512 (2011).

[10]E. Preciado, F. J. Schulein, A. E. Nguyen, D. Barroso, M. Isarraraz, G. von Son, I. H. Lu, W. Michailow, B. Moller, V. Klee, J. Mann, A. Wixforth, L. Bartels, and H. J. Krenner, Nat. Commun. **6**, 8593 (2015).

[11]M. L. Zhang, W. W. Cui, X. J. Chen, C. Wang, W. Pang, X. X. Duan, D. H. Zhang, and H. Zhang, J. Micromech. Microeng. **25**(2), 025002 (2015).

[12]J. Liang, H. X. Zhang, H. Xie, W. Pang, D. H. Zhang, and H. Zhang, in *Proceedings of IEEE International Frequency Control Symposium*, 2014, p. 114.

[13]X. S. Li, Y. W. Zhu, W. W. Cai, M. Borysiak, B. Y. Han, D. Chen, R. D. Piner, L. Colombo, and R. S. Ruoff, Nano Lett. **9**(12), 4359 (2009).

[14]S. Rumyantsev, G. Liu, M. S. Shur, R. A. Potyrailo, and A. A. Balandin, Nano Lett. **12**(5), 2294 (2012).

[15]G. S. Kulkarni, K. Reddy, Z. Zhong, and X. Fan, Nat. Commun. **5**, 4376 (2014).

[16]A. S. Mayorov, N. Hunter, W. Muchenje, C. D. Wood, M. Rosamond, E. H. Linfield, A. G. Davies, and J. E. Cunningham, Appl. Phys. Lett. **104**(8), 083509 (2014).

[17]M. Rotter, A. Wixforth, W. Ruile, D. Bernklau, and H. Riechert, Appl. Phys. Lett. **73**(15), 2128 (1998).

[18]D. Chen, J. J. Wang, D. H. Li, Y. Xu, and Z. X. Li, Sens. Actuators, A **165**(2), 379 (2011).